Research on Chemical Intermediates (2026) 52:1211–1238
https://doi.org/10.1007/s11164-025-05854-4

Photocatalytic antibiotic degradation efficiency of g-C_3N_4 prepared from waste melamine–formaldehyde

Hafize Nagehan Koysuren[1] · Sumyah Amer Yahya[2] · Ozcan Koysuren[2]

Received: 18 October 2025 / Accepted: 2 December 2025 / Published online: 16 December 2025

Abstract

Graphitic carbon nitride (g-C_3N_4) was synthesized by applying a thermal treatment using waste melamine–formaldehyde product as a precursor. Photocatalytic antibiotic degradation performances of g-C_3N_4 was investigated. To enhance the photocatalytic activity of g-C_3N_4, the heat treatment temperature was varied as an experimental variable during the synthesis of g-C_3N_4, and different proportions of urea and silica template materials were separately mixed with the precursor before the heat treatment. A higher degree of crystallization was obtained as the heat treatment temperature was increased. According to FTIR analysis, it was understood that g-C_3N_4 was obtained more successfully at the heat treatment temperature of 650 °C. Mixing the precursor with urea and silica template did not significantly affect the chemical structure of the resulting g-C_3N_4. Mixing waste melamine–formaldehyde product with silica template gave rise to approximately sixfold expansion in the BET surface area of g-C_3N_4. It was determined that the g-C_3N_4 particles obtained by mixing waste melamine–formaldehyde product with urea and silica template turned from irregular blocks to spherical structures and the particle size decreased. By mixing waste melamine–formaldehyde product with urea and silica template, the photocatalytic antibiotic degradation efficiency of the resulting g-C_3N_4 was enhanced. The highest photocatalytic degradation efficiency (41.9%) was obtained on g-C_3N_4 synthesized from waste melamine–formaldehyde precursor containing urea and silica template under UV light irradiation for 120 min. It was attempted to produce high-value-added photocatalyst from waste melamine–formaldehyde material, reflecting the originality of the present study.

Keywords g-C_3N_4 · Photocatalyst · Antibiotics · Photocatalytic activity · Tetracycline

Extended author information available on the last page of the article

Introduction

Water pollution caused by industrial wastewater threatens aquatic wildlife and human life. Among various water pollutants, drugs, heavy metal ions, and organic dyes are highly toxic to human health even at low concentrations. Therefore, effective treatment approaches are needed to reduce these pollutants in water in order to protect human health and the ecosystem [1]. Compared to various drugs, antibiotics are considered as an important pollutant due to their widespread use [2]. The presence of antibiotics in the aquatic environment leads to environmental problems due to their toxicological effects and biological activities [3]. The widespread use of antibiotics leads to the easy transfer of antimicrobial resistance genes among bacterial species. The presence of antimicrobial resistance genes weakens the ability to control and prevent infectious diseases, threatening human health. Therefore, the removal of antibiotics from the aquatic environment is of great importance [2]. Even if antibiotics are not directly discharged into water resources, they can affect public health by mixing with surface water and groundwater depending on the rate of diffusion in the soil [4].

Various techniques such as flocculation [5], ion exchange [6], membrane filtration [7], adsorption [8], electro-Fenton process [9], photo-Fenton [9], sonocatalytic degradation [10] and photocatalytic degradation [8] have been applied for the removal of antibiotics from wastewater. In recent years, there has been great interest in the use of advanced oxidation processes in wastewater treatment due to their environmental friendliness and high efficiency. Among the specified traditional techniques, photocatalytic degradation has attracted great interest due to its economic nature and simple processes. This technique has been recognized as one of the green processes to degrade antibiotics using UV or visible light irradiations [11].

Graphitic carbon nitride (g-C_3N_4) has been known as a narrow band gap (2.7 eV) photocatalyst that can be synthesized by simple methods using non-toxic and cheap raw materials. Being a metal-free semiconductor, g-C_3N_4 has high stability even in acidic or alkaline environments because of its suitable electronic structure. However, g-C_3N_4 also has some disadvantages, such as low surface area, high electron–hole recombination rate and low quantum efficiency [12]. Especially, the morphology of the synthesized g-C_3N_4 has a great significance to obtain high photocatalytic antibiotic removal efficiency. The low surface area of g-C_3N_4 seriously limits the photocatalytic activity. The low surface area makes it difficult for the photogenerated electron–hole pairs to transfer to the surface and increases the mass transfer resistance during the photocatalytic reaction. Therefore, it is important to obtain a high surface area and porous structure for better photocatalytic activity [13]. The heat treatment temperature applied during the synthesis of g-C_3N_4 from its precursor also has a significant effect on the morphology, crystal structure and optical properties of the photocatalyst. Zhang and his coworkers (2013) studied the effect of the heat treatment temperature in the range of 300–650 °C to obtain g-C_3N_4 from melamine. As the heat treatment temperature increased, the polymeric structure of the g-C_3N_4 was extended by

binding more tri-s-triazine molecules and the bond length of the sp^2 C-N structures increased, resulting in an increase in the sp^2 C-N structures. The increase in the dimensions of the mentioned sp^2 structures led to a narrowing of the optical band gap from 3.1 eV to 2.4 eV [14]. In a similar comprehensive study, Yadav and his coworkers (2021) synthesized g-C_3N_4 through the heat treatment of melamine. The effect of the heat treatment temperature (550–650 °C) on the morphology and optical properties of the prepared photocatalyst was investigated. The sample prepared at 600 °C provided a higher specific surface area (25.5 m^2/g) with a narrower optical band gap (2.7 eV) [15].

The main structure of g-C_3N_4 is the tri-s-triazine ring clusters, which are connected to each other by nitrogen atoms to form a π-conjugated polymeric network structure [14]. The main precursors or raw materials used to prepare g-C_3N_4 are melamine, urea and cyanamide. g-C_3N_4 can be synthesized by thermal condensation of these precursor materials. If melamine is selected as the precursor material, the intermediate product, melem, is obtained through thermal condensation of melamine. Then, the specified intermediate product is converted g-C_3N_4 through melon formation. If urea is selected as the precursor material, it is initially converted to melamine by thermal condensation and elimination of NH_3. Then, g-C_3N_4 is obtained by ring formation reactions and the release of CO_2 and H_2O gases [16]. In the literature, g-C_3N_4 has been synthesized by heat treatment of many different precursor materials containing carbon and nitrogen atoms. In this context, g-C_3N_4 was obtained in powder form by heat treatment of thiourea [17, 18], urea, melamine [18], urea-melamine formaldehyde resin [19] and protonated melamine [13].

The precursor materials have also been mixed and used to synthesize g-C_3N_4. Especially, mixing the precursor like melamine with urea can enhance the specific surface area of the product g-C_3N_4. In addition, mixing the precursor material with urea before the heat treatment process leads to the formation of point defects in the final product. Mostly, N vacancies are observed in the bulk g-C_3N_4 structure. The enhancement in the specific surface area and the point defect formation by urea addition are important to improve the photocatalytic antibiotic degradation efficiency. A large surface area is essential to provide additional reaction sites on the catalyst. On the other hand, the point defects can act as electron–hole trapping sites, suppressing the recombination of the photoinduced charge carriers on the catalyst [16]. In the literature, Nakagawa and his coworkers (2024) prepared g-C_3N_4 from melamine/urea mixtures. The photocatalytic formaldehyde decomposition rate obtained by g-C_3N_4, synthesized from the melamine/urea mixture, was almost 3 times as high as that of g-C_3N_4, synthesized from pure melamine. The enhancement in the photocatalytic activity was attributed to the enlarged specific surface area and the formation of point defects. At least a two-fold increase in the specific surface area of g-C_3N_4 was observed by mixing melamine with urea before the heat treatment process [16]. In another study in the literature, Negro and his coworkers (2024) prepared g-C_3N_4 using a mixture precursor with a weight ratio of melamine/urea (1:1). Compared to g-C_3N_4 prepared using pure melamine, approximately fourfold increase in the specific surface area of g-C_3N_4 was achieved. The release of CO_2 during the thermal condensation of the mixture precursor, including urea, might be the reason for the larger surface area. The photocatalytic dye degradation rate increased at least

1.5-fold with g-C_3N_4 prepared using the melamine/urea mixture [20]. In a similar study, Niu and his coworkers (2023) synthesized g-C_3N_4 through the heat treatment of a dual precursor, melamine/urea, with different weight ratios. The specific surface area of g-C_3N_4 prepared from the mixture precursor with a weight ratio of 1:4 (melamine/urea) was 33.2 m^2/g, which was almost 2.5-fold higher than that of g-C_3N_4 prepared from pure melamine. The photocatalytic dye degradation performance of g-C_3N_4 synthesized from the mixture precursor was improved by almost 60% compared to g-C_3N_4 prepared from pure melamine. The higher specific surface area provided stronger adsorption ability and more active sites on g-C_3N_4, leading to the mentioned improvement in the photocatalytic dye degradation performance [21].

Synthesis of g-C_3N_4 with a porous surface structure can expand the accessible and active surface area of photocatalyst, which can promote mass transfer of reactants to the surface and removal of reaction products from the surface. Porous surface structure also promotes the surface reactions due to the enhanced surface area. In addition, light-harvesting ability of g-C_3N_4 can be enhanced with the porous surface structure. The photoexcited charge carriers can be separated more easily on the porous surface of the photocatalyst. The mentioned benefits of the porous surface structure can enhance the photocatalytic performance of g-C_3N_4 [22]. Surface porosity on g-C_3N_4 can be obtained by template methods. In the literature, Zhang and his coworkers (2019) obtained surface porosity on g-C_3N_4 by using silica nanoparticles as a template material in the melamine precursor. With the silica template application, the BET surface area of g-C_3N_4 increased by approximately 6 times and the photocatalytic dye removal rate increased by 13 times [22]. Shen and his coworkers (2017) synthesized porous g-C_3N_4 by mixing the cyanamide precursor with SiO_2 nanoparticles as the template material. The silica template expanded the specific surface area of g-C_3N_4 from 11 m^2/g to 19 m^2/g. The photocatalytic dye degradation efficiency of g-C_3N_4 was improved from 10 to 58% under visible light irradiation [23]. Hao and his coworkers (2016) prepared g-C_3N_4 nanoparticles using melamine and silica nanoparticles as the precursor and the template material. The BET surface area was expanded from 8.7 m^2/g to 14.0 m^2/g with the silica template application. The presence of the silica nanoparticles might expand the specific surface area by intercalating between g-C_3N_4 sheets. The photocatalytic dye degradation efficiency of g-C_3N_4 was improved from 40 to 60% within 100 min of visible light irradiation [24]. In another study, Chen and his coworkers (2020) prepared a porous g-C_3N_4 photocatalyst using silica nanoparticles as the template material. The BET surface area of the photocatalyst sample with silica template reached about 160 m^2/g, which was about 11 times the surface area of g-C_3N_4 prepared without a template material. The expanded surface area might provide more active sites, promoting the photocatalytic hydrogen evolution rate [25].

To date, many researchers have conducted studies to synthesize g-C_3N_4 from different precursor materials, but none have published a report on synthesizing g-C_3N_4 from waste melamine–formaldehyde products. Melamine–formaldehyde is produced by the polymerization of melamine and formaldehyde. It is a type of thermosetting resin with high porosity and a three-dimensional network structure. Due to its properties such as light weight, heat resistance, flame retardancy, corrosion resistance, and flexibility, it has been widely used in kitchen products, household cleaning

products, acoustic equipment, fire prevention materials, and other fields in recent years. With the rapid development of the construction industry, the consumption of melamine–formaldehyde is also increasing rapidly [26]. As a result, a large number of waste melamine–formaldehyde products accumulate in our environment, not only occupying agricultural land but also seriously polluting the environment. Due to the environmental problems caused by thermosetting resin waste, it is important to dispose of melamine–formaldehyde or convert it into a usable product. In this study, the waste melamine–formaldehyde product was converted into g-C_3N_4 catalyst through a heat treatment. The heat treatment temperature applied during the synthesis of g-C_3N_4 was varied as an experimental variable. Furthermore, the effect of mixing the melamine–formaldehyde precursor with urea and silica template on the morphology, crystal structure and especially photocatalytic performance of g-C_3N_4 was investigated.

Experimental

Materials and methods

To synthesize g-C_3N_4, waste melamine–formaldehyde kitchenware was utilized. The melamine–formaldehyde kitchenware was broken into small pieces by using a hammer. They were then ground into powder using a grinder (IKA 10 A basic). The precursor melamine–formaldehyde powder was converted to g-C_3N_4 nanoparticles by a heat treatment. The precursor powder was placed in a ceramic crucible and heated in a tube furnace (Protherm, PTF Series) with a heating rate of 5°/min until it reached the desired temperature. Then, it was held at this temperature for 4 h under a nitrogen atmosphere. After cooling, the resulting product was ground in a mortar to obtain pure g-C_3N_4 nanoparticles [27]. The heat treatment temperature applied to obtain g-C_3N_4 powder was changed as an experimental parameter. Waste melamine–formaldehyde powder was heated in the furnace at three different temperatures (550 °C, 600 °C, 650 °C) for 4 h. The heat treatment temperature was expected to affect both the crystal structure and the photocatalytic activity of the resulting g-C_3N_4 powder [15]. In order to distinguish among the g-C_3N_4 samples, they were labeled as g-C_3N_4(T) (T = 550 °C, 600 °C, 650 °C). The heat treatment temperature with the highest antibiotic removal efficiency was determined by photocatalytic activity tests and the optimum heat treatment temperature was used in follow-up studies.

As an experimental parameter, urea was added to the waste melamine–formaldehyde powder. A certain amount of urea (Sigma-Aldrich) (5, 10 and 15% by weight of melamine–formaldehyde) was dissolved in 100 ml of distilled water. Then, a certain amount of the ground melamine–formaldehyde powder was mixed with urea in its solution and stirred for 1 h. Afterward, water was removed at room temperature by natural evaporation and the powder sample was then dried in an oven at 100 °C. Finally, the powder was heated in the tube furnace at the optimum temperature for 4 h. The resulting powder was ground into powder for further use [18]. Urea application was expected to affect both the surface area and the photocatalytic activity

of the resulting g-C_3N_4 powder. The g-C_3N_4 powder including urea was named as g-C_3N_4(T,x) (x = 5 wt.%, 10 wt.%, 15 wt.% urea). The optimum urea content of the mixture precursor (waste melamine–formaldehyde/urea) providing the highest photocatalytic activity of g-C_3N_4 was attempted to be determined and used in subsequent studies.

Before the heat treatment at the optimum temperature, a certain amount of SiO_2 nanoparticles (15–35 nm, Nanografi) as template material (5 wt.%, 10 wt.% and 15 wt. % of the melamine–formaldehyde powder) was physically mixed with waste melamine–formaldehyde powder, including urea. Then, the heat treatment was applied for 4 h at the optimum temperature. After the heat treatment, the powder sample was washed with hydrofluoric acid (10%) to separate the SiO_2 template material from the structure. After the g-C_3N_4 powder was separated from the hydrofluoric acid solution by filtration and washing, it was dried in the oven at 100 °C [22]. The application of the SiO_2 template was expected to affect both the surface area and photocatalytic activity of the resulting g-C_3N_4 powder. The as-prepared g-C_3N_4 sample was denoted as g-C_3N_4(T,x,y) (y = 5 wt.%, 10 wt.%, 15 wt.% SiO_2). The optimum SiO_2 composition of g-C_3N_4 providing the highest photocatalytic activity was determined.

Structural, morphological and optical characterization

The specific surface area and the pore structure of the prepared g-C_3N_4 were measured by adsorption/desorption of N_2 using an Autosorb-6 model analyzer (Quantachrome Corporation) based on the Brunner–Emmett–Teller (BET) method and the Barret-Joyner-Halender (BJH) method, respectively. Fourier-transform infrared (FTIR) spectroscopy of the catalyst samples was recorded using a Bruker IFS 66/S model spectrophotometer between 4000–400 cm^{-1}. X-ray diffraction (XRD) patterns of the powder samples were collected using a Rigaku Ultima IV model X-ray diffractometer at a scan rate of 1°/min with Cu Kα irradiation. QUANTA 400F model field emission scanning electron microscope (FESEM) was used to investigate the morphology of the obtained g-C_3N_4. The optical absorption spectrum of the catalyst samples was recorded by a UV–Vis spectrophotometer (Genesys 10S, Thermo Scientific). X-ray photoelectron spectroscopy (XPS) measurement of g-C_3N_4 was performed on a PHI 5000 VersaProbe model spectrometer. The photoluminescence spectrum of the catalyst samples was recorded on a Jobin Yvon Flooring-550 model spectrophotometer.

Characterization of the photocatalytic performance

The photocatalytic activity of the as-prepared samples was evaluated by monitoring the degradation of a model antibiotic, tetracycline, under UV light irradiation. 25 mg of the photocatalyst sample was dispersed in 50 ml of tetracycline solution (5 mg/l). The as-prepared suspension was stirred for half an hour using a magnetic stirrer in the dark to reach adsorption/desorption equilibrium. Then, the suspension was exposed to the UV light irradiation (12 W, UVA light). The suspension was stirred using the magnetic stirrer while exposed to the UVA light irradiation. Every

20 min., 2 ml of the suspension was extracted and centrifuged to separate photocatalyst particles from the tetracycline solution. Then, the antibiotic concentration of the residual solution was determined using the UV–Vis spectrophotometer by monitoring the absorbance at 358 nm. The antibiotic degradation rate was calculated using the following Eq. (1). In addition, the following pseudo-first-order kinetic model (2) was used to study the reaction kinetics of the antibiotic degradation.

$$\%\ \text{degradation} = \left(C_0 - C\right) / C_0 \text{x}\ 100 \tag{1}$$

$$\ln\left(C_0/C\right) = kt \tag{2}$$

where C_0 is the concentration of tetracycline before irradiation and C is the concentration of tetracycline after the UVA light irradiation. The reaction rate constant (k) was determined from the slope of the $\ln(C_0/C)$ vs. t graph of the samples. The solution concentration of tetracycline was changed between 1 mg/L and 10 mg/L to investigate the effect of the initial solution concentration on the photocatalytic performance of g-C_3N_4. In addition, the catalyst concentration of the antibiotic solution was changed between 0.1 g/L and 1 g/L to study the effect of the initial catalyst concentration on the photocatalytic performance. The initial pH of the antibiotic solution was adjusted to 3, 5, 9 and 11 by using HCl and NaOH, respectively, to investigate the effect of ambient pH on the photocatalytic performance. On the other hand, to understand the formation mechanism of active radicals on g-C_3N_4, tert-butanol (6 ml/100 ml) and ascorbic acid (1 mg/100 ml) were added into the tetracycline solution to trap hydroxyl (•OH) radical and superoxide ($\bullet O_2^-$) radical, respectively. In addition to the simulated tetracycline solutions prepared using distilled water, it was planned to investigate the photocatalytic tetracycline degradation efficiency of g-C_3N_4(650,15,10) in a real wastewater sample obtained from Ankara Central Wastewater Treatment Plant. The real wastewater experiment was similar to that of the simulated tetracycline solution experiment, except for the utilization of wastewater instead of distilled water. In addition, five subsequent degradation cycles were performed to study the stability and reusability g-C_3N_4. The mineralization ratio of the tetracycline solution exposed to the UVA light irradiation was determined by using a Shimadzu TOC-L model total organic carbon (TOC) analyzer.

Results and discussion

XRD analysis

On the XRD pattern of all samples (Fig. 1), two characteristic diffraction peaks of g-C_3N_4 were present at 27.4° and 13.1°, attributed to the (002) plane and (100) plane, respectively (JCPDS 87–1526). The strongest peak at the diffraction angle of 27.4° was associated with the inter-layer stacking of the melem plane [15, 28]. The diffraction peak present at 13.1° was associated with the tri-s-triazine-based intralayer structural unit [15, 28]. According to Fig. 1a-1c, the intensity of the strongest peak increased as the heat temperature increased from 550 °C to 650 °C, indicating

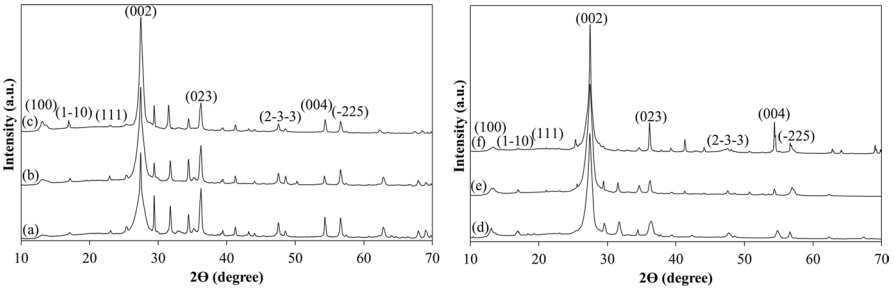

Fig. 1 XRD diffractogram of **a** g-C_3N_4(550), **b** g-C_3N_4(600), **c** g-C_3N_4(650), **d** g-C_3N_4(650,5), **e** g-C_3N_4(650,15) and **f** g-C_3N_4(650,15,10)

that a higher degree of crystallization was obtained along the (002) plane [15]. In addition, the characteristic diffraction peak at 27.4° indicated the formation of a graphitic structure [15]. It was understood that the g-C_3N_4 structure was obtained to a certain extent at all heat treatment temperatures. On the other hand, there were additional diffraction peaks that did not belong to the g-C_3N_4 structure, at around 17.1°, 23.1°, 34.4°, 36.2°, 39.4°, 47.6° and 56.6° (Fig. 1a-1c), assigned to the (1–10), (111), (211), (023), (1–31), (2–3-3) and (-225) planes of melamine–formaldehyde, respectively (JCPDS 39–1950) [29, 30]. The presence of the diffraction peaks belonging to the crystalline structure of melamine–formaldehyde indicated that there was still a certain amount of unreacted melamine–formaldehyde in the g-C_3N_4 structure. In addition, there were prominent peaks at 25.4°, 48.6°, 54.3°, 62.8° and 69.1°, assigned to the (002), (101), (004), (110) and (112) planes of graphite, which might be formed during the heat treatment of the melamine–formaldehyde precursor [31]. While an increase in the intensity of the characteristic peaks of g-C_3N_4 was detected with the increase in the heat treatment temperature, a decrease in the intensity of the peaks of unreacted melamine–formaldehyde was detected. The mean domain size (Dp) was calculated from Scherrer's equation [20]:

$$\mathrm{Dp} = (0.9\lambda) / (\beta \cos\theta) \tag{3}$$

where λ was the X-ray wavelength, β was full width at half maximum of the most intense peak, θ was the diffraction angle. The mean crystal size of g-C_3N_4(550), g-C_3N_4(600) and g-C_3N_4(650) was calculated as 15.81 nm, 11.23 nm and 14.47 nm, respectively. The calculations revealed that there were fluctuations in the mean domain size as the heat treatment temperature increased.

Figure 1d and 1e exhibited the XRD patterns of the g-C_3N_4 samples, prepared from melamine–formaldehyde/urea mixture. The peak intensities at 13.1° and 27.4° increased with the addition of urea to the precursor of g-C_3N_4, indicating a change in the original crystal structure of g-C_3N_4 synthesized from the waste melamine–formaldehyde product. The peak position associated with the tri-s-triazine-based intralayer structural unit did not show any shift with the addition of urea to the precursor. On the other hand, there was a slight shift in the peak position at 27.4° towards lower diffraction angles. The mentioned shift of the peak at 27.4° towards lower diffraction angles indicated an increase in the inter-layer distance in g-C_3N_4. Therefore,

the addition of urea to the melamine–formaldehyde precursor led to an exfoliation in the as-prepared catalyts [16]. Similar to the XRD pattern of g-C_3N_4(650), diffraction peaks belonging to crystalline graphite and melamine–formaldehyde were also present on the XRD pattern of g-C_3N_4(650,5) and g-C_3N_4(650,15), indicating that the prepared catalyst did not consist of only g-C_3N_4. The mean domain size of g-C_3N_4(650,5) and g-C_3N_4(650,15) was calculated as 10.81 nm and 9.48 nm, respectively. Compared with the average domain structure of g-C_3N_4(650), a slight shrinkage was observed in the mean domain structures of g-C_3N_4(650,5) and g-C_3N_4(650,15). Smaller domain size values might be an indication of pore formation [32]. With the addition of urea, g-C_3N_4 might transform into a porous structure, leading to a smaller domain size value.

To identify the effect of silica template to the crystal structure g-C_3N_4, XRD pattern of g-C_3N_4(650,15,10) was also collected (Fig. 1f). As seen in Fig. 1f, the characteristic peaks of g-C_3N_4(650,15,10) did not show any shift compared to the characteristic peaks found in the XRD pattern of g-C_3N_4(650,15), indicating that the silica template did not change the original crystal structure of g-C_3N_4(650,15) much. On the other hand, there was an increase in the peak intensity of g-C_3N_4(650,15,10) at 27.4°, indicating a high level of aggregation or a growth in average size of crystallite domains in the orthorhombic g-C_3N_4 structure [20]. It was observed that the peaks of g-C_3N_4(650,15) at 29.4° and 31.6° disappeared in the XRD pattern of g-C_3N_4(650,15,10) and the intensity of the peaks at 36.2° and 54.3° increased. Other peaks belonging to the crystalline melamine–formaldehyde and graphite were still present in the XRD pattern of g-C_3N_4(650,15,10). The mean domain size of g-C_3N_4(650,15,10) was calculated as 25.11 nm, which was greater than that of g-C_3N_4(650,15). Silica with its large surface area could act as a nucleating agent during the heat treatment process and promote the growth of crystal structures in g-C_3N_4.

FTIR analysis

Figure 2 illustrated FTIR spectra of g-C_3N_4 synthesized at two different temperatures. Figure 2 also illustrated FTIR spectra of g-C_3N_4 synthesized from different precursor mixtures. All of the samples exhibited similar transmittance peaks between 1200 and 1700 cm^{-1}. The characteristic peaks present at around 1230 cm^{-1}, 1315 cm^{-1}, 1402 cm^{-1} and 1460 cm^{-1} were corresponded to the aromatic C–N stretching vibrations, whereas the characteristic peaks at around 1550 cm^{-1} and 1625 cm^{-1} were attributed to C = N stretching vibrations [33]. In addition, the sharp transmittance peak at around 823 cm^{-1} was assigned to the breathing mode of s-triazine units. The broad transmittance band between 2800 – 3600 cm^{-1} was corresponded to N–H stretching and O–H stretching vibrations of g-C_3N_4 [33]. All of the samples exhibited all the characteristic peaks of g-C_3N_4, indicating that g-C_3N_4 was successfully synthesized under all conditions. On the other hand, g-C_3N_4(550) had a broad transmittance peak at around 1776 cm^{-1}, which was assigned to C = O stretching vibrations [33]. The intensity of the mentioned peak declined as the heat treatment temperature of g-C_3N_4 increased from 550 °C to 650 °C. The reason for the

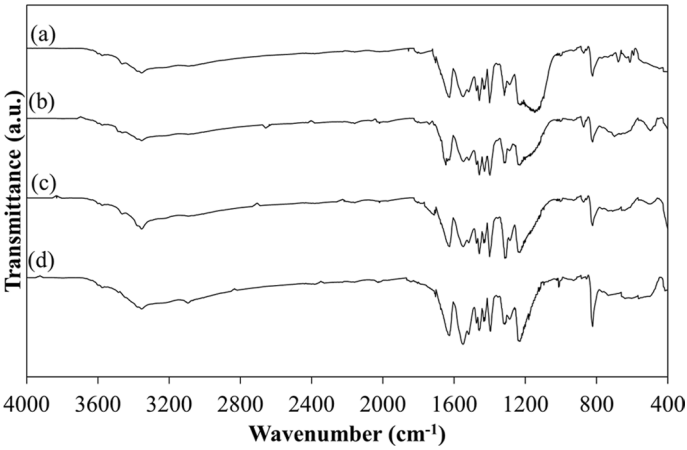

Fig. 2 FTIR spectrum of **a** g-C_3N_4(550), **b** g-C_3N_4(650), **c** g-C_3N_4(650,15) and **d** g-C_3N_4(650,15,10)

emergence of this peak might be the presence of isocyanic acid as an intermediate product formed during the synthesis of g-C_3N_4. The peak of C = O stretching vibrations was very weak in the FTIR spectra of g-C_3N_4(650,15) and g-C_3N_4(650,15,10), which revealed that the conversion efficiency from melamine–formaldehyde to g-C_3N_4 was higher at 650 °C in the presence of urea and silica nanoparticles. In addition, there was an intense peak at around 1135 cm^{-1} in the FTIR spectrum of g-C_3N_4(550). The mentioned peak weakened and disappeared with the samples synthesized at the heat treatment temperature of 650 °C. There were different types of carbon-containing functional units in the melamine–formaldehyde structure. These units might transform into an amorphous carbon matrix instead of adding to the graphite-like layer structure of g-C_3N_4 [34]. It might be the reason for the observed peak at about 1135 cm^{-1} in the FTIR spectrum of g-C_3N_4(550). Compared with g-C_3N_4(650), no significant differences were observed in the spectral patterns of g-C_3N_4(650,15) and g-C_3N_4(650,15,10). It was found that the use of urea together with melamine–formaldehyde for the synthesis of g-C_3N_4 or the addition of silica nanoparticles to the waste melamine–formaldehyde did not significantly affect the chemical structure of the resulting product.

XPS analysis

The surface chemical composition of g-C_3N_4 was investigated by XPS. The survey scanned XPS spectrum of g-C_3N_4(650,15,10) illustrated C1s and N1s peaks (Fig. 3a). The surface chemical composition of g-C_3N_4(650,15,10) was illustrated in Table 1. It was understood that the N/C atom ratio of g-C_3N_4(650,15,10) was lower than the theoretical N/C atom ratio. During the heat treatment process, nitrogen atoms might leach from the surface structure of g-C_3N_4(650,15,10), causing nitrogen atom defects in the surface structure [34]. The high-resolution XPS spectrum of C1s of g-C_3N_4(650,15,10) exhibited two main peaks at 284.7 eV and 288.3 eV, respectively (Fig. 3b). The peak at 284.7 eV was thought to originate from carbon

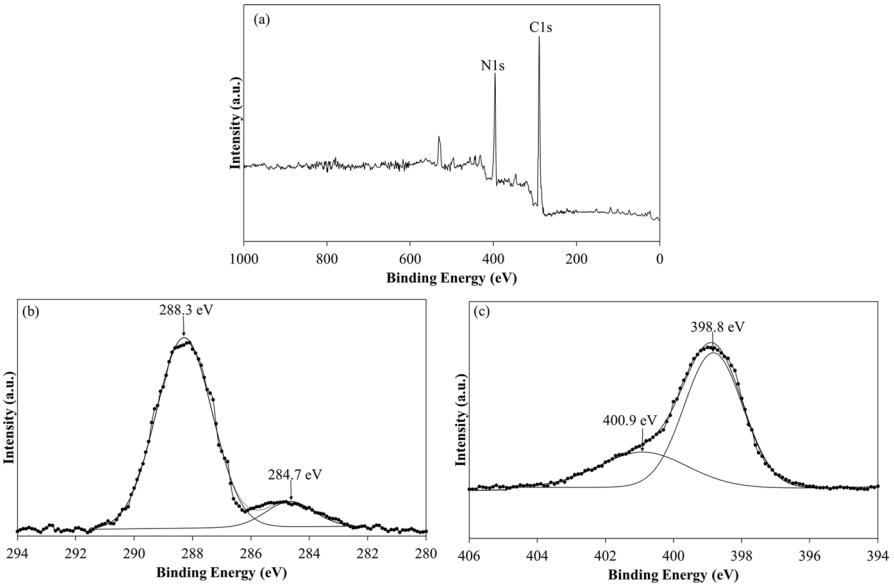

Fig. 3 XPS spectra of g-C_3N_4(650,15,10): **a** full scan, **b** C1s and (c) N1s

Table 1 Compositions of C and N (wt.%) in the sample obtained by the XPS analysis

Sample	C (wt.%)	N (wt.%)	O (wt.%)
g-C_3N_4(650,15,10)	66.2	27.3	6.5

atoms deposited on the surface structure or C–C bonds in the graphitic carbon structure [34, 35]. The second peak might be due to N–C = N bonds in the g-C_3N_4 structure [34, 35]. The high-resolution XPS spectrum of N1s of g-C_3N_4(650,15,10) included two main peaks at 398.8 eV and 400.9 eV (Fig. 3c), which were attributed to tertiary nitrogen groups (C-N = C) and -NH_x groups in g-C_3N_4, respectively [34, 35]. Both the survey scanned XPS spectrum and the high resolution XPS spectrum of C1s and N1s of g-C_3N_4(650,15,10) confirmed the successful conversion of waste melamine–formaldehyde into g-C_3N_4.

N_2 adsorption and desorption analysis

To investigate the specific surface area of g-C_3N_4 catalysts, nitrogen adsorption–desorption measurements were performed. According to Fig. 4a-f, all the samples followed the type IV isotherm with a distinct capillary condensation step at high pressures, which was assigned to a mesoporous structure [22]. Additionally, the hysteresis loops were of type H3, which was attributed to the formation of slit-shaped pores from clusters of plate-like particles [36]. Figure 4a and 4b exhibited the N_2 adsorption–desorption isotherm of g-C_3N_4 samples synthesized at two

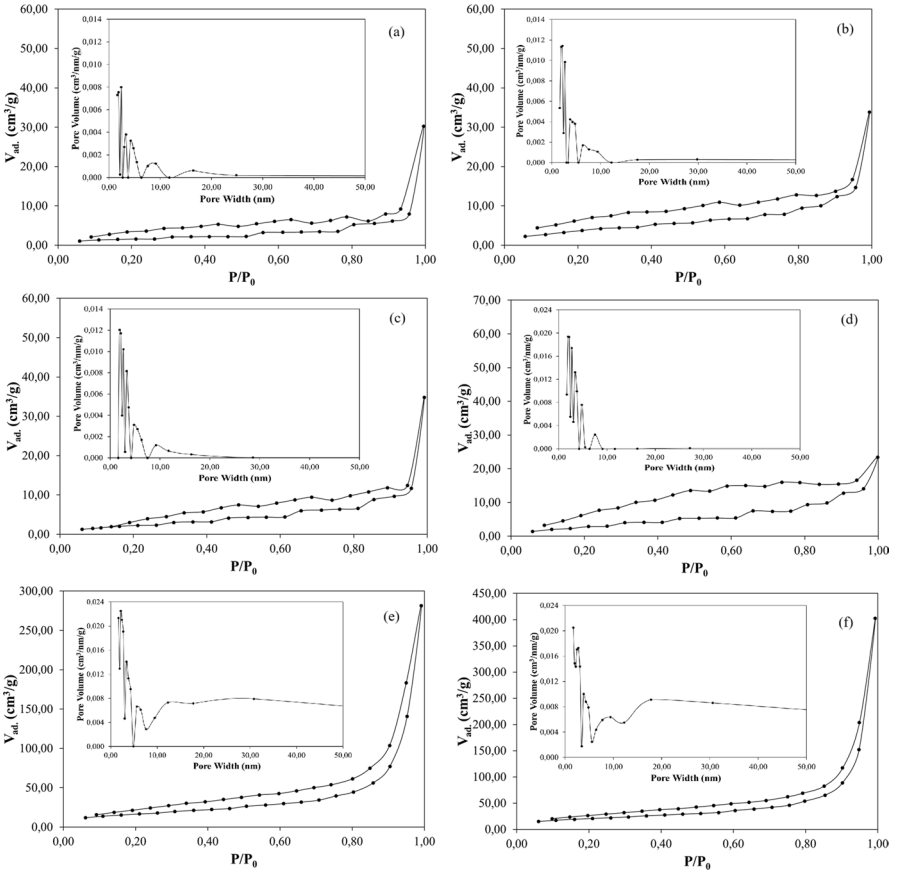

Fig. 4 N_2 adsorption–desorption isotherm (Inset plots exhibit the BJH pore size distribution) for **a** g-C_3N_4(550), **b** g-C_3N_4(650), **c** g-C_3N_4(650,5), **d** g-C_3N_4(650,15), **e** g-C_3N_4(650,15,5) and **f** g-C_3N_4(650,15,10)

Table 2 Surface area and pore size data according to BET and BJH methods

Sample	BET Surface Area (m^2/g)	Pore Volume (cm^2/g)	Average Pore Size (nm)
g-C_3N_4(550)	5.89	0.055	2.39
g-C_3N_4(650)	14.52	0.057	2.13
g-C_3N_4(650,5)	9.16	0.064	1.88
g-C_3N_4(650,15)	10.51	0.050	1.89
g-C_3N_4(650,15,5)	60.24	0.453	2.15
g-C_3N_4(650,15,10)	73.69	0.634	1.68

different heat treatment temperatures. The specific surface area of g-C_3N_4(550) and g-C_3N_4(650) was calculated to be 5.89 m^2/g and 14.52 m^2/g, respectively. The specific surface area increased in parallel with the increase in the heat treatment temperature (Table 2). The average pore diameter decreased as the heat treatment temperature increased (Table 2). With an increase in the heat treatment temperature, the polymeric network of the g-C_3N_4 might grow by the addition of more tri-s-triazine units, leading to an increase in the specific surface area and pore volume [14].

Figure 4c and 4d illustrated the N_2 adsorption–desorption isotherm of g-C_3N_4 samples synthesized from melamine–formaldehyde/urea mixtures. Compared with g-C_3N_4(650), g-C_3N_4(650,5) and g-C_3N_4(650,15) exhibited smaller specific surface areas of 9.16 m^2/g and 10.51 m^2/g, respectively, with corresponding pore sizes of 1.88 nm and 1.89 nm (Table 2). During the heat treatment of urea, CO_2 might form and be released from the bulk structure. The release of CO_2 might form structural defects in the final product. It was expected that urea in the precursor material would increase the specific surface of g-C_3N_4 due to the formation of the structural defect [37]. Contrary to expectation, a decrease in specific surface area was observed with the addition of urea to the waste melamine–formaldehyde precursor.

The adsorption–desorption isotherms of g-C_3N_4 synthesized in the presence of silica nanoparticles were illustrated in Fig. 4e and 4f. The BET surface area of g-C_3N_4(650,15,5) and g-C_3N_4(650,15,10) was greater than that of g-C_3N_4(650,15), indicating the enhanced surface area by the silica nanoparticles as the template material. By removing the silica nanoparticles from the g-C_3N_4 structure, a more porous microstructure might be achieved, leading to the enhanced surface area. Approximately sixfold expansion in the BET surface area and ninefold increase in the pore volume were achieved by the silica template (Table 2). An enhanced surface area could provide more active sites for the photocatalytic redox reactions and was therefore beneficial for the photocatalytic applications. In this context, the application of silica nanoparticles as a template material was found to be significant and successful in expanding the specific surface area of g-C_3N_4.

Optical characteristics

The optical properties of all photocatalyst samples were examined using UV–Vis spectroscopy. The absorption spectrum of g-C_3N_4(550), g-C_3N_4(600) and g-C_3N_4(650) exhibited an absorption band between 300 and 400 nm (Fig. 5a-5c). As the heat treatment temperature increased from 550 °C to 650 °C, the spectrum of g-C_3N_4 showed a blue shift in the absorption band. g-C_3N_4(550) exhibited an additional absorption peak at approximately 480 nm. As the heat treatment temperature increased, the specified peak disappeared. Fig. S1 illustrated the Tauc plot of g-C_3N_4(550), g-C_3N_4(600) and g-C_3N_4(650), respectively. The heat treatment temperature applied for the synthesis of g-C_3N_4 had a significant effect on the optical band gap value. It was understood that increasing the heat treatment temperature widened the optical band gap. The absorption spectrum of g-C_3N_4(650,5), g-C_3N_4(650,10) and g-C_3N_4(650,15) exhibited a broad absorption band starting from 400 to 300 nm (Fig. 5d-5f). The absorption peak observed in

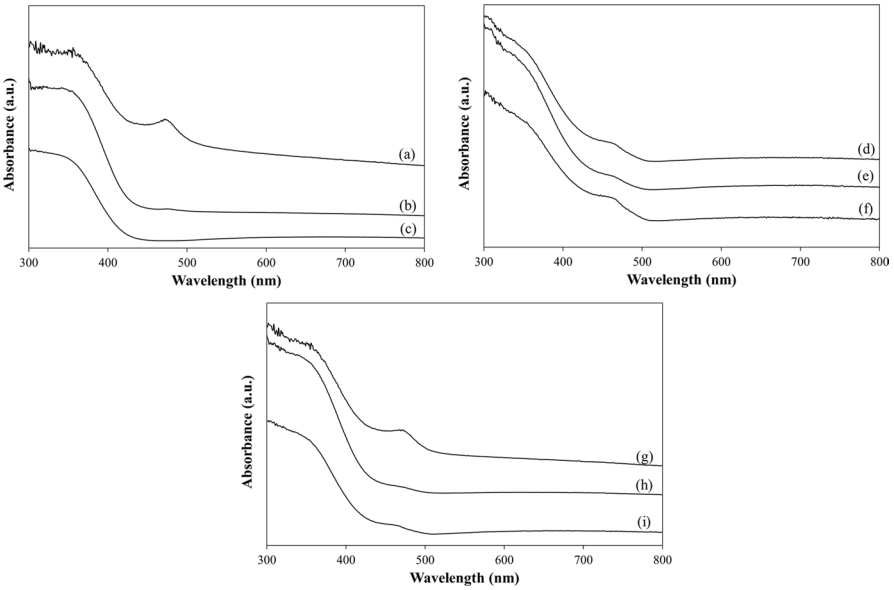

Fig. 5 UV–Vis absorbance spectrum of **a** g-C_3N_4(550), **b** g-C_3N_4(600), **c** g-C_3N_4(650), **d** g-C_3N_4(650,5), **e** g-C_3N_4(650,10), **f** g-C_3N_4(650,15), **g** g-C_3N_4(650,15,5), **h** g-C_3N_4(650,15,10) and **i** g-C_3N_4(650,15,15)

the spectrum of g-C_3N_4(550) at around 480 nm was also observed in the spectrum of g-C_3N_4(650,5), g-C_3N_4(650,10) and g-C_3N_4(650,15). Fig. S2 presented the Tauc plot of g-C_3N_4(650,5), g-C_3N_4(650,10) and g-C_3N_4(650,15), respectively. The g-C_3N_4 samples obtained from melamine–formaldehyde/urea precursor exhibited narrower optical band gaps compared to g-C_3N_4(650). It was understood that the addition of urea into the melamine–formaldehyde precursor also had a significant effect on the optical band gap and optical features. The absorption spectrum of g-C_3N_4(650,15,5), g-C_3N_4(650,15,10) and g-C_3N_4(650,15,15) also exhibited a broad absorption band starting from 400 to 300 nm (Fig. 5g-5i). It was found that the silica template added to the precursor material for the g-C_3N_4 synthesis did not have a significant effect on the optical properties of the resulting material. The optical band gap energy of g-C_3N_4(650,15,5), g-C_3N_4(650,15,10) and g-C_3N_4(650,15,15) was estimated to be 2.75, 2.85 and 2.85 eV, respectively (Fig. S3). Moreover, the silica content in the precursor material did not change the optical band gap energy much.

To reveal the effect of the synthesis procedure on the photocatalytic performance of the obtained photocatalyst, the photoluminescence (PL) spectrum of g-C_3N_4(550) and g-C_3N_4(650,15,10) were recorded and compared in Fig. S4. The main emission peak of the samples was noticed at around 450 nm. The peak intensity of g-C_3N_4(650,15,10) was lower than that of g-C_3N_4(550), indicating a lower recombination rate of the photoinduced charge carriers on g-C_3N_4(650,15,10). The reduction in the recombination rate of the photoinduced electron–hole pairs might promote the photocatlytic tetracycline degradation.

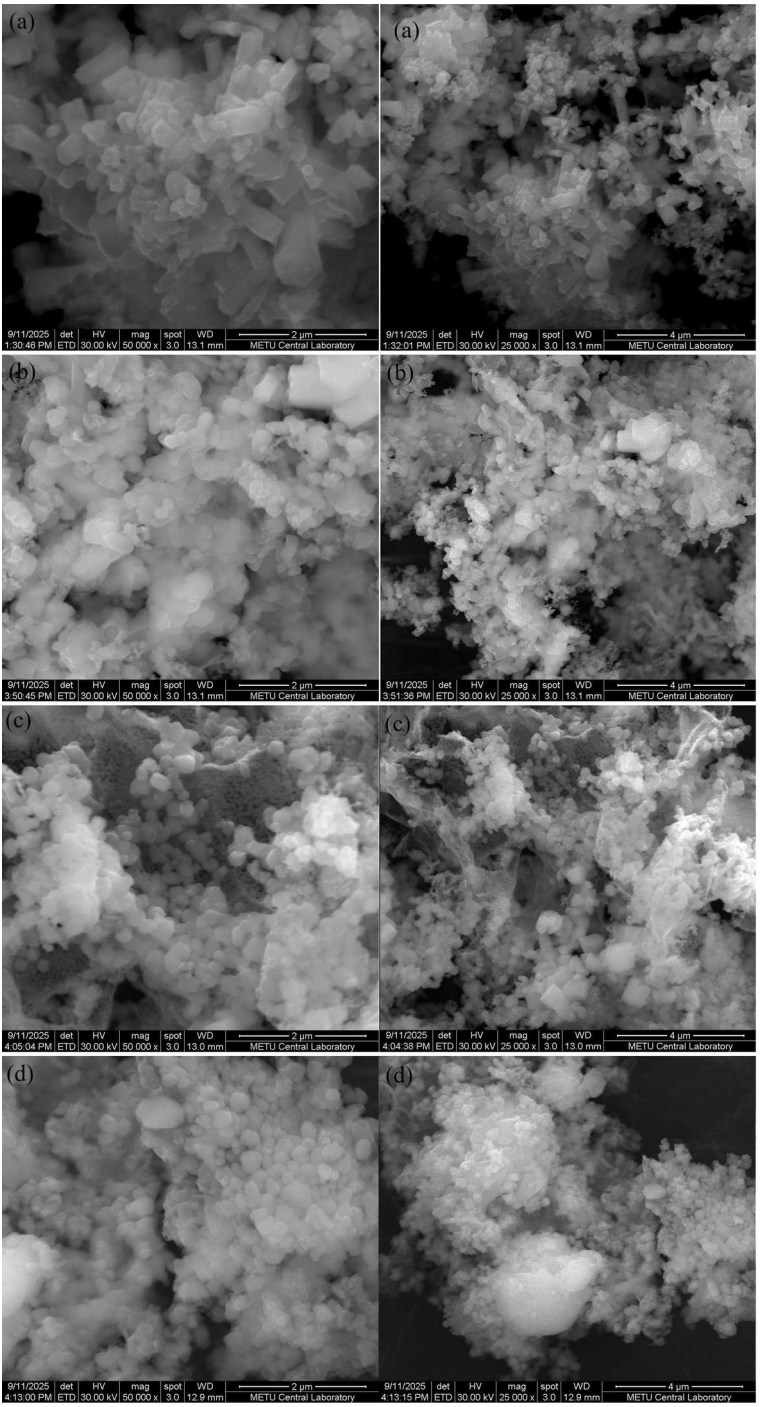

Fig. 6 FESEM images of **a** g-C_3N_4(550), **b** g-C_3N_4(650), **c** g-C_3N_4(650,15) and **d** g-C_3N_4(650,15,10)

Morphology analysis

FESEM analysis was performed to investigate the morphology of g-C_3N_4, synthesized under different process conditions. As shown in Fig. 6a, g-C_3N_4 (550) exhibited irregular thick blocks. Wang and co-workers (2017) also observed irregular block structures in FESEM images of g-C_3N_4 synthesized from melamine precursor [38]. Similar to g-C_3N_4(550), g-C_3N_4(650) also revealed irregular block structures (Fig. 6b). It was understood that increasing the heat treatment temperature from 550 °C to 650 °C did not have a significant effect on the morphology of the obtained g-C_3N_4. There was a slight decrease in the average particle size of g-C_3N_4. The g-C_3N_4 samples synthesized from waste melamine–formaldehyde precursor exhibited a morphology based on stacked blocks with dimensions between 1 µm and 2 µm; whereas the g-C_3N_4 sample synthesized from melamine–formaldehyde/urea mixture exhibited a morphology based on agglomerates of spherical particles with dimensions between 200 nm and 1 µm. It was understood that the g-C_3N_4 particles obtained by heat treatment of melamine–formaldehyde/urea mixture were more homogeneous and spherical in structure (Fig. 6c). On the other hand, g-C_3N_4, synthesized in the presence of the silica template, also exhibited agglomerates of spherical particles (Fig. 6d). During the heat treatment of the mixture precursor, silica templates might act as a seed, promoting the growth of g-C_3N_4 on their surface. Spherical g-C_3N_4 nanoparticles with sizes of 200–400 nm were obtained by the heat treatment of the mixture precursor in the presence of silica templates. More uniform and smaller g-C_3N_4 nanoparticles were obtained using the silica template. The decrease in the particle size also meant an increase in the specific surface area required for enhanced photocatalytic activity. Luo and co-worker (2016) also obtained spherical g-C_3N_4 nanoparticles from the calcination of melamine with the silica template [39].

Photocatalytic performance of g-C_3N_4

The photocatalytic activity of g-C_3N_4 samples was evaluated by the degradation of tetracycline under UV light irradiation. Fig. S5 illustrated UV–Vis absorption spectra of tetracycline in the presence of g-C_3N_4 nanoparticles synthesized in three different heat treatment temperatures. In general, the absorption intensity decreased with time under the UVA light irradiation. The photocatalytic antibiotic degradation efficiency of the as-prepared samples was illustrated in Fig. 7. g-C_3N_4(650) exhibited higher photocatalytic antibiotic degradation efficiency compared to g-C_3N_4(550) and g-C_3N_4(600). 20.2% of tetracycline was degraded within 120 min after exposure to the UVA light. The enhancement of photocatalytic antibiotic degradation efficiency within the temperature range of 550 to 650 °C might be due to a gradual increase in the specific surface area and the crystallinity of g-C_3N_4 nanoparticles. The enhanced photocatalytic activity of g-C_3N_4(650) could be assigned to two phenomena. First, the high specific surface area of g-C_3N_4(650) might enhance the adsorption capacity of g-C_3N_4(650) nanoparticles to target antibiotic molecules, which promoted the

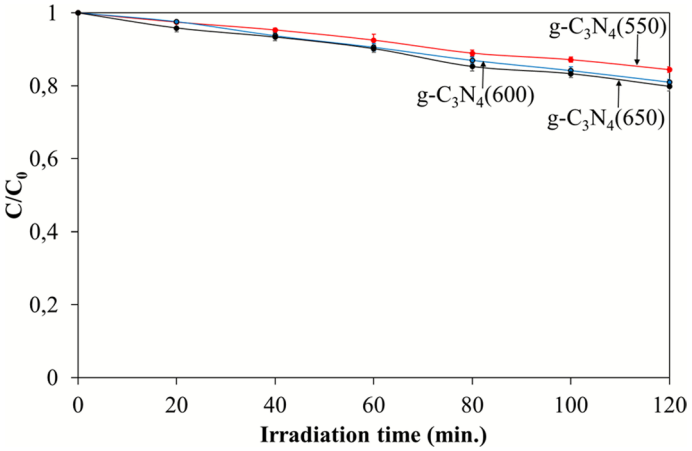

Fig. 7 The photocatalytic tetracycline degradation efficiency of g-C_3N_4 synthesized at three different heat treatment temperatures

interaction of g-C_3N_4 with the antibiotic molecules, and thus improved the antibiotic degradation efficiency of the catalyst. Second, with the growth of the crystal structure, the electron–hole pairs generated by the photoexcitation of g-C_3N_4 could more easily flow from the bulk structure of the catalyst to its surface [7].

The reaction rate constant (k) values, obtained from Fig. S6, were presented in Table 3. As expected, g-C_3N_4(650) provided higher k value than that of g-C_3N_4(550) and g-C_3N_4(600). The highest reaction rate constant value obtained by g-C_3N_4(650) was almost 1.4 times as high as that of g-C_3N_4(550). According to high R^2 values close to 1, the reaction kinetics of photocatalytic tetracycline degradation over the catalyst samples seemed to fit the pseudo-first order kinetics model. The optimum heat treatment temperature providing the highest photocatalytic activity was determined as 650 °C and used in subsequent studies.

Fig. S7 illustrates UV–Vis absorption spectra of tetracycline in the presence of g-C_3N_4 nanoparticles synthesized using three different melamine–formaldehyde/urea compositions. Figure 8 exhibits the time course of tetracycline degradation efficiency over the three samples. The tetracycline solution, including g-C_3N_4 nanoparticles synthesized using melamine–formaldehyde/urea mixtures underwent slightly higher degradation. g-C_3N_4(650,15) exhibited the highest photocatalytic tetracycline degradation efficiency among the three samples. 26.3% tetracycline was removed from the solution by g-C_3N_4(650,15) under the UVA light irradiation (Fig. 8). The melting and the decomposition temperatures of melamine and urea are different, which might alter

Table 3 Adjusted parameters of the pseudo-first-order kinetic model

Sample	k (min^{-1})	R^2
g-C_3N_4(550)	0.0014	0.9940
g-C_3N_4(600)	0.0017	0.9958
g-C_3N_4(650)	0.0019	0.9936

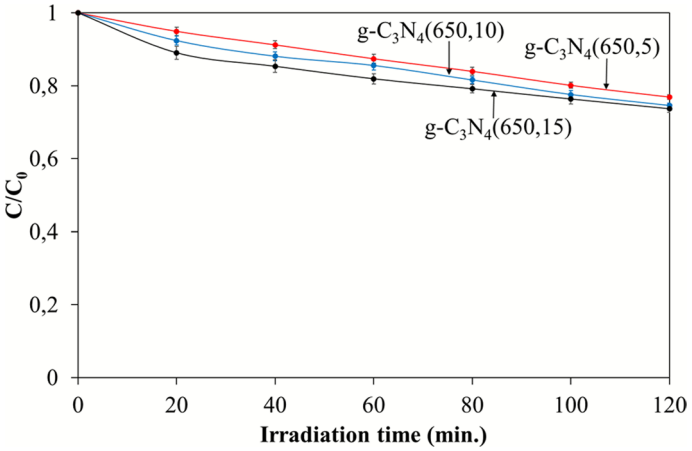

Fig. 8 The photocatalytic tetracycline degradation efficiency of g-C_3N_4 synthesized using three different melamine–formaldehyde/urea mixtures

the polymerization behavior of melamine–formaldehyde to form g-C_3N_4 nanoparticles. The decomposable and volatile features of urea might serve as bubble templates, preventing agglomeration of melamine–formaldehyde in the polymerization process at high temperatures. Thus, g-C_3N_4 with a small particle size might be obtained [22]. According to the XRD and FESEM analyses, there was a slight decrease in the mean particle size of g-C_3N_4 synthesized from melamine–formaldehyde/urea mixtures. Also, there was an improvement in the crystal structure of g-C_3N_4 obtained from melamine–formaldehyde/urea mixtures. By improving the crystal structure, electron–hole pairs formed on g-C_3N_4 could be transferred to the catalyst surface more easily [7]. The strategy of combining melamine–formaldehyde with urea before the heat treatment process appeared to be successful and increased the photocatalytic tetracycline degradation efficiency. In addition, an increase in the tetracycline removal efficiency was observed in parallel with the increase in the amount of urea in the melamine–formaldehyde/urea mixture used for the g-C_3N_4 synthesis. The optimum urea content of melamine–formaldehyde/urea mixtures providing the highest photocatalytic activity was determined as 15 wt.% (g-C_3N_4(650,15)) and used in subsequent studies.

The reaction rate constant values, determined from the slope of the plot of $\ln(C_0/C_t)$ vs. irradiation time t (Fig. S8), were presented in Table 4. According to Table 3 and 4, the rate of tetracycline degradation increased when urea was combined with the waste melamine–formaldehyde precursor to synthesize g-C_3N_4 nanoparticles. Besides, increasing the urea content of the melamine–formaldehyde/urea mixtures also

Table 4 Adjusted parameters of the pseudo-first-order kinetic model

Sample	k (min^{-1})	R^2
g-C_3N_4(650,5)	0.0022	0.9983
g-C_3N_4(650,10)	0.0026	0.9743
g-C_3N_4(650,15)	0.0028	0.8766

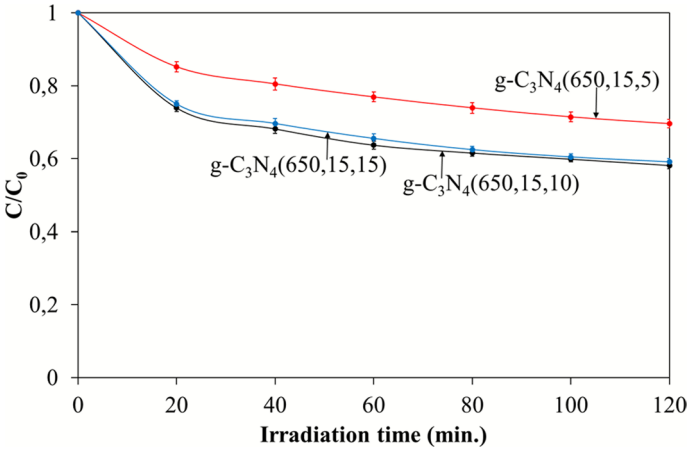

Fig. 9 The photocatalytic tetracycline degradation efficiency of g-C_3N_4 synthesized using the mixture precursor with three different silica template compositions

Table 5 Adjusted parameters of the pseudo-first-order kinetic model

Sample	k (min^{-1})	R^2
g-C_3N_4(650,15,5)	0.0035	0.7779
g-C_3N_4(650,15,10)	0.0056	0.5470
g-C_3N_4(650,15,15)	0.0054	0.5909

enhanced the photocatalytic tetracycline degradation rate of the catalyst. The highest reaction rate constant value obtained by g-C_3N_4(650,15) was almost 1.3 times as high as that of g-C_3N_4(650,5).

Fig. S9 illustrated the absorption changes of tetracycline during the photocatalytic degradation reaction in the presence of g-C_3N_4 synthesized using the optimum melamine–formaldehyde/urea mixture with three different silica template compositions. When the silica template composition was compared, a slight difference in the peak intensity of the absorption spectrum was detected under the UVA light irradiation. Figure 9 exhibited the photocatalytic performance of the three different catalysts towards tetracycline. 30.4% tetracycline degradation was obtained over g-C_3N_4(650,15,5) within 120 min of UVA light irradiation. The photocatalytic tetracycline degradation efficiency of g-C_3N_4(650,15,10) and g-C_3N_4(650,15,15) enhanced to 41.9% and 40.9%, respectively. According to the photocatalytic tetracycline degradation results, g-C_3N_4(650,15,10) provided slightly higher photocatalytic activity. Silica template decreased the mean particle size and enlarged the specific surface area of g-C_3N_4, which could increase the number of active sites on g-C_3N_4 and enhance the photocatalytic tetracycline degradation efficiency [23].

The reaction rate constants, obtained from Fig. S10, were illustrated on Table 5. The reaction kinetics of photocatalytic degradation of tetracycline revealed incorporating silica nanoparticles with the mixture precursor used to synthesize g-C_3N_4 improved the photocatalytic reaction rate. The reaction rate constant for

g-C_3N_4(650,15,5) was about 1.2 times higher than that for g-C_3N_4(650,15). Compared to g-C_3N_4(650,15,5), an approximately 1.4-fold increment in the reaction rate constant was obtained with g-C_3N_4(650,15,10).

The complete mineralization of tetracycline molecules in distilled water in the presence of g-C_3N_4(650,15,10) was studied by measuring the total organic carbon (TOC) content. After 120 min, the total organic carbon (TOC) of tetracycline mineralization value was 27.6% for g-C_3N_4(650,15,10). The complete mineralization rate at the end of the photocatalytic degradation reaction was found to be lower than the photocatalytic tetracycline removal rate, which was related to the fact that all the antibiotic molecules were not completely mineralized and were decomposed into smaller carbon-based products.

In the literature, photocatalytic activity studies conducted with g-C_3N_4 have not achieved very high tetracycline removal due to the low surface area and high electron–hole recombination rate of g-C_3N_4. In the study conducted by Zhao et al. (2019), approximately 40% photocatalytic tetracycline removal was achieved [19]. Unlike studies in the literature, this study attempted to obtain g-C_3N_4 from waste melamine–formaldehyde product. Chemical and morphological characterization studies indicated that g-C_3N_4 was successfully obtained. Achieving photocatalytic tetracycline removal slightly above the literature data with g-C_3N_4 obtained from a waste product constitutes the unique aspect of this study.

To reveal the adsorption effect of the antibiotic molecules on the photocatalytic degradation performance, the tetracycline removal experiment was also performed in the absence of UV light. 13.1% tetracycline was removed from the solution by g-C_3N_4(650,15,10) within 120 min in the dark (Fig. S11). It was understood that the surface adsorption process contributed to the photocatalytic tetracycline removal to a certain extent. Similarly, to reveal the effect of photolysis on the photocatalytic degradation performance, the tetracycline removal experiment was also performed in the absence of the photocatalyst under UV light irradiation. Only 7.8% tetracycline was removed from the solution within 120 min under the UV light irradiation (Fig. S12). It was found that the contribution of photolysis to the photocatalytic tetracycline degradation was negligible.

Effect of initial antibiotic concentration on photocatalytic performance

Figure 10a illustrated the effect of varying tetracycline solution concentration on the photocatalytic performance of g-C_3N_4(650,15,10). With an increase in the initial tetracycline solution concentration from 1.0 mg/L to 5.0 mg/L, the photocatalytic tetracycline degradation efficiency of g-C_3N_4(650,15,10) increased from 38.8% to 41.9%. The increase in the photocatalytic degradation efficiency with increasing tetracycline solution concentration might be attributed to the increase in the number of antibiotic molecules that could be adsorbed on the catalyst surface [40, 41]. Further increasing the concentration of the tetracycline solution caused the photocatalytic degradation efficiency to decrease to 34.1% (Fig. 10a). More intermediate products might be produced and accumulated during the photocatalytic degradation reaction. The reaction intermediates might compete with the photogenerated active species,

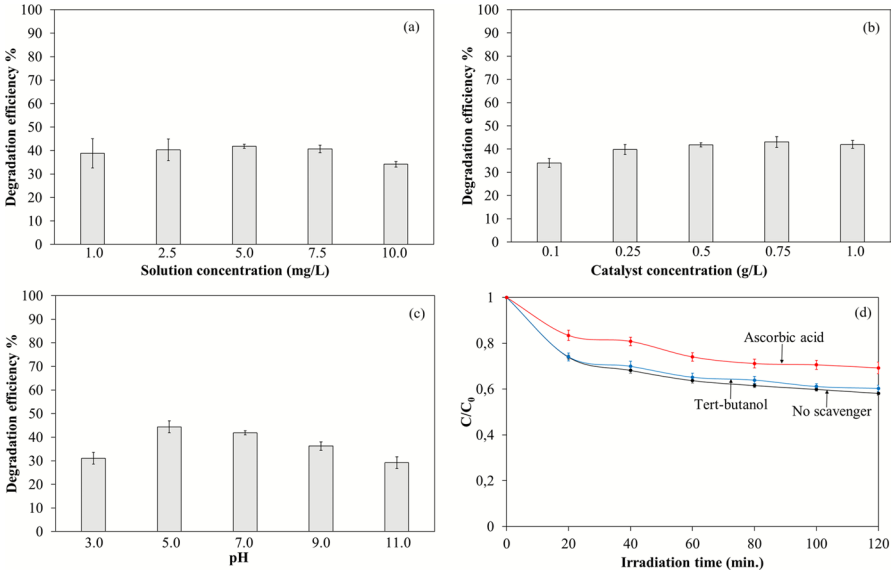

Fig. 10 **a** Effect of the initial concentration of the antibiotic solution, **b** effect of the initial catalyst concentration, **c** effect of the initial solution pH and **d** effect of superoxide and hydroxyl radical scavengers on the tetracycline degradation efficiency of g-C_3N_4(650,15,10)

suppressing the photocatalytic degradation of tetracycline [40, 41]. In addition, if the solution concentration of tetracycline is too high, the light transmittance of the antibiotic solution might decrease and the production rate of photoexcited charge carriers on the catalyst might be suppressed. Thus, the photocatalytic performance of the catalyst could be affected [40].

Effect of initial catalyst concentration on photocatalytic tetracycline degradation

The effect of varying catalyst concentration on the photocatalytic tetracycline degradation efficiency was illustrated in Fig. 10b. When the initial catalyst concentration was between 0.1 g/L and 1 g/L, the photocatalytic tetracycline degradation efficiency in the presence of g-C_3N_4(650,15,10) was 34.1%, 39.8%, 41.9, 43.0% and 42.0%, respectively. The catalyst concentration of 0.75 g/L for g-C_3N_4(650,15,10) exhibited higher photocatalytic performance. As the catalyst concentration increased from 0.1 g/L up to the optimum value, the photocatalytic tetracycline degradation efficiency was enhanced. The reason for this enhancement was ascribed to the increase in active sites on the photocatalyst to generate more reactive species. Further increasing the catalyst concentration negatively affected the photocatalytic degradation efficiency. Excessive amounts of catalyst in the tetracycline solution might lead to agglomeration of the catalyst particles, or it could reduce light penetration, creating a more turbid solution. The agglomeration of the photocatalyst or a turbid

solution might reduce the amount of light absorbed and slow down the rate of formation of photoinduced charge carriers on the catalyst sample [40].

Effect of initial solution pH on photocatalytic tetracycline degradation

The pH value of the solution could affect and change the surface charge of the catalyst and the pollutant molecules, thus determining the adsorption rate of the pollutant molecules on the catalyst surface. Figure 10c illustrated the photocatalytic degradation rates of tetracycline at varying initial solution pH. When the initial solution pH value was adjusted to 3, 5, 7, 9 and 11, the photocatalytic tetracycline degradation efficiency of g-C_3N_4(650,15,10) was 31.0%, 44.4%, 41.9%, 36.2% and 29.2%, respectively (Fig. 10c). The highest removal rate for the catalyst sample was obtained when the initial solution pH was adjusted to 5.0. When the initial solution pH value was less than 3.3, tetracycline molecules existed as cations [40]. The surface of g-C_3N_4(650,15,10) might be positively charged when the initial solution pH value was less than 3.3. Thus, the adsorption and the photocatalytic degradation rate of tetracycline on the catalyst surface might be suppressed. In addition, very low pH values might reduce the photocatalytic degradation efficiency by preventing the formation of superoxide radicals in tetracycline solution [40]. When the initial solution pH value was between 3.3 and 7.7, tetracycline molecules existed as zwitterion [40]. In this pH range, an electrostatic attraction between tetracycline molecules and catalyst particles was expected to start and increase, which might be the reason for the highest removal rates at the pH value of 5.0. When the initial solution pH value was greater than 7.7, tetracycline molecules existed as anion [40]. The surface of g-C_3N_4(650,15,10) might be negatively charged when the initial solution pH value was greater than 7.7. An electrostatic repulsion between the antibiotic molecules and catalyst particles was expected to start, preventing adsorption of tetracycline molecules onto the catalyst surface. Therefore, alkaline solution condition did not promote either the adsorption or photocatalytic degradation of tetracycline on g-C_3N_4(650,15,10).

Active species trapping experiments and photocatalytic mechanism

To determine the active species in the photocatalytic tetracycline degradation reactions, trapping experiments were performed using tert-butanol as hydroxyl radical (•OH) scavenger and ascorbic acid as superoxide radical ($\bullet O^{2-}$) scavenger. The effect of scavengers on the photocatalytic tetracycline degradation performance of g-C_3N_4(650,15,10) was illustrated in Fig. 10d. According to the trapping experiments results, the photocatalytic degradation efficiency of tetracycline over g-C_3N_4(650,15,10) decreased from 41.9% to 39.7%, when tert-butanol was used as hydroxyl radical scavenger, while the photocatalytic degradation efficiency of tetracycline over g-C_3N_4(650,15,10) decreased from 41.9% to 30.8%, when ascorbic acid was added into the tetracycline solution (Fig. 10d). The trapping experiments revealed that $\bullet O^{2-}$ was the main active radical responsible for the photocatalytic degradation of tetracycline over g-C_3N_4(650,15,10). On the basis of the results of

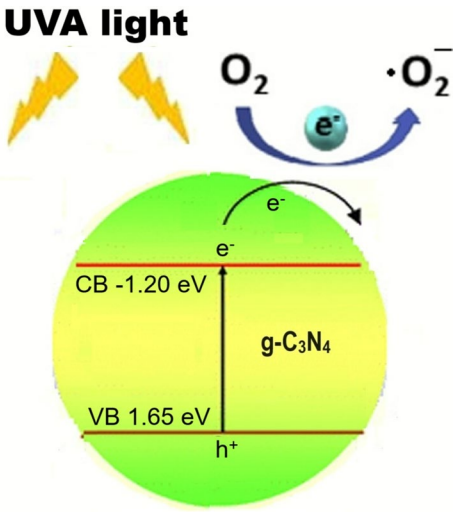

Fig. 11 Formation mechanism of photoexcited charge carriers on the g-C_3N_4(650,15,10) under UVA light irradiation

the trapping experiments, an acceptable degradation mechanism of tetracycline over the catalyst sample was proposed and illustrated in Fig. 11. The edge potentials of the conduction band and valence band for g-C_3N_4(650,15,10) were calculated using the following relations [42]:

$$E_{CB} = X - E^{e} - 0.5E_{g} \tag{4}$$

$$E_{VB} = E_{CB} + E_{g} \tag{5}$$

where E_{CB} and E_{VB} were the edge potentials of the conduction band and valence band, respectively. E^{e} is the energy of free electrons (4.5 eV) on the hydrogen scale. According to the Tauc plot analysis, E_g (optical band gap) value for g-C_3N_4(650,15,10) was found to be 2.85 eV. In addition, X is the absolute electronegativity of the catalyst [42]. The value of the absolute electronegativity (X) was calculated as 4.73 for g-C_3N_4(650,15,10). The edge potentials of the conduction band and valence band for g-C_3N_4(650,15,10) were found out to be -1.20 eV and 1.65 eV, respectively. UVA light could excite the valence band electrons of g-C_3N_4(650,15,10), which led to the formation of photogenerated electron–hole pairs. The conduction band edge potential of g-C_3N_4(650,15,10) was more negative than the standard reduction potential of O_2 to form superoxide radicals (-0.33 eV vs. NHE), Hence, the photoexcited electrons of g-C_3N_4(650,15,10) could react with O_2 to form superoxide radicals [43, 44]. On the other hand, the standard redox potential of H_2O/•OH (2.27 eV vs. NHE) was more positive than the valence band edge potential of g-C_3N_4(650,15,10). Hence, the photogenerated holes of g-C_3N_4(650,15,10) could not react with surface-adsorbed water molecules to form •OH radicals [43, 44]. Therefore, $•O^{2-}$ might be the main active species for the degradation of tetracycline. The active species trapping experiments also supported the proposed degradation mechanism.

Real wastewater application and reusability performance of photocatalysts

To investigate the effects of a real wastewater environment on the photocatalytic performance of g-C_3N_4, the photocatalytic degradation of tetracycline added into a real wastewater sample was also examined. When real wastewater was used instead of distilled water to prepare the antibiotic solution, 37.2% tetracycline degradation was obtained in the presence of g-C_3N_4(650,15,10) (Fig. 12a). The photocatalytic tetracycline degradation efficiency of g-C_3N_4(650,15,10) decreased by about 4% in the real wasterwater environment. The decrease in the photocatalytic degradation efficiency was assigned to the reduction in the effective surface area required for the antibiotic degradation. The pollution present in the wastewater might adsorb onto the photocatalyst surface, reducing the surface area required for the photocatalytic degradation reaction.

The reusability of a photocatalyst is indeed important and determine its potential for practical application in wastewater treatment. The photocatalytic tetracycline degradation performance of recycled g-C_3N_4(650,15,10), which was separated from the solution, washed with distilled water and dried after the degradation reaction, was evaluated to reveal the reusability of the catalyst sample. The photocatalytic tetracycline degradation efficiency over recycled g-C_3N_4(650,15,10) reduced from 41.9% to 32.8% after five cycles (Fig. 12b), indicating that there was no significant decrease in the photocatalytic performance of the catalyst sample with the consecutive photocatalytic degradation cycles.

Conclusions

The present study provided a well-known catalyst for the photocatalytic antibiotic degradation activity by the heat treatment of a waste product. In this study, it was aimed to obtain g-C_3N_4 nanoparticles from waste melamine–formaldehyde products. The novelty of the study was to obtain a photocatalyst from a waste product. One of the biggest problems of the g-C_3N_4 synthesis is that the resulting material has low surface area and low photocatalytic activity. It was observed that increasing

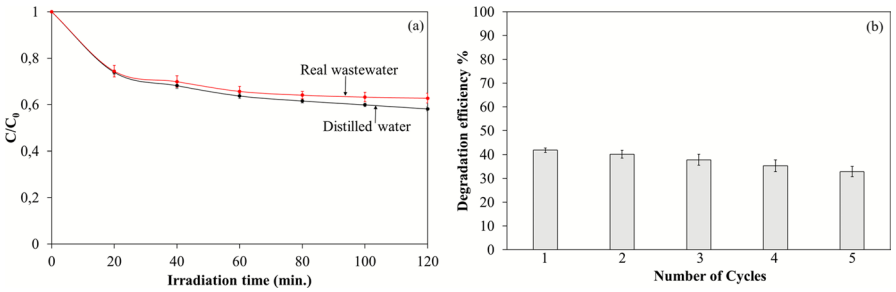

Fig. 12 **a** The photocatalytic tetracycline degradation efficiency of g-C_3N_4(650,15,10) in distilled water and real wastewater solutions, **b** repetitive cycles of photocatalytic tetracycline degradation over g-C_3N_4(650,15,10)

the heat treatment temperature applied to the waste melamine–formaldehyde precursor and mixing the precursor with urea and silica templates improved the crystal structure of the resulting g-C_3N_4, increased its surface area, and reduced its particle size. Especially, the photocatalytic tetracycline degradation efficiency of the as-prepared catalyst could be optimized by changing the process parameters used to synthesize g-C_3N_4. Hence, g-C_3N_4(650,15,10) provided the best photocatalytic tetracycline degradation performance (41.9%). The photocatalytic tetracycline degradation efficiency of g-C_3N_4(650,15,10) did not exhibit a significant reduction in the real wastewater environment (37.2%) and after five consecutive cycles of photocatalytic degradation experiments (32.8%). In conclusion, pure g-C_3N_4 obtained from a waste product can be considered as a promising catalyst for photocatalytic degradation of antibiotics and other organic compounds in wastewater.

Supplementary Information The online version contains supplementary material available at https://doi.org/10.1007/s11164-025-05854-4.

Acknowledgements The authors are thankful to The Scientific and Technological Research Council of Türkiye (TÜBİTAK) for the research grant 224M345.

Author contributions All authors contributed to the study conception and design. Material preparation, data collection and analysis were performed by Hafize Nagehan Koysuren, Sumyah Amer Yahya Yahya and Ozcan Koysuren.

Funding This research has been supported by The Scientific and Technological Research Council of Türkiye (TÜBİTAK) with the Project Number 224M345.

Data Availability No datasets were generated or analysed during the current study.

Declarations

Conflict of interest The authors declare no competing interests.

References

1. S. Hu, H. Wang, F. Wang, J. Bai, L. Zhang, X. Kang, G. Wu, G., Practical preparation of carbon black/carbon nitride compounds and their photocatalytic performance. Bull. Korean Chem. Soc. **36**(10), 2527 (2015)
2. P. Gholami, L. Dinpazhoh, A. Khataee, A. Hassani, A. Bhatnagar, Facile hydrothermal synthesis of novel Fe-Cu layered double hydroxide/biochar nanocomposite with enhanced sonocatalytic activity for degradation of cefazolin sodium. J. Hazard. Mater. **381**, 120742 (2020)
3. S. Dehghan, B. Kakavandi, R.R. Kalantary, Heterogeneous sonocatalytic degradation of amoxicillin using ZnO@ Fe3O4 magnetic nanocomposite: influential factors, reusability and mechanisms. J. Mol. Liq. **264**, 98 (2018)
4. N.Y. Tizhoosh, A. Khataee, R. Hassandoost, R.D.C. Soltani, E. Doustkhah, Ultrasound-engineered synthesis of WS2@ CeO2 heterostructure for sonocatalytic degradation of tylosin. Ultrason. Sonochem. **67**, 105114 (2020)
5. X. Tang, W. Fan, S. Zhang, B. Yan, H. Zheng, The improvement of levofloxacin and tetracycline removal from simulated water by thermosensitive flocculant: mechanisms and simulation. Sep. Purif. Technol. **309**, 123027 (2023)
6. L. Nicoud, K.V. Gonzalez, A. Portier, R.M. Nicoud, Using mechanistic modeling for understanding antibiotics purification with ion exchange chromatography. Solvent Extr. Ion Exch. **38**(5), 555 (2020)

7. Y. Li, H. Sun, T. Peng, X. Qing, Effect of temperature on the synthesis of g-C3N4/montmorillonite and its visible-light photocatalytic properties. Clays Clay Miner. **70**(4), 555 (2022)
8. T. Yu, T. Zeng, F. Shi, J. Liu, X. Tian, C. Ma, Constructing a novel mesoporous CsxWO3/C composite aerogel for efficient adsorption/photocatalytic degradation of Oxytetracycline. J. Solid State Chem. **314**, 123411 (2022)
9. X. Liu, Y. Zhou, J. Zhang, L. Luo, Y. Yang, H. Huang, H. Peng, L. Tang, Y. Mu, Insight into electro-Fenton and photo-Fenton for the degradation of antibiotics: mechanism study and research gaps. J. Chem. Eng. **347**, 379 (2018)
10. A. Noypha, Y. Areerob, S. Chanthai, P. Nuengmatcha, Fe_2O_3-graphene anchored Ag nanocomposite catalyst for enhanced sonocatalytic degradation of methylene blue. J. Korean Ceram. Soc. **58**, 297 (2021)
11. Z.F. Gu, Y.J. Xu, B. Hong, J.C. Xu, Y.B. Han, H.X. Jin, D.F. Jin, X.L. Peng, J. Gong, H.L. Ge, X.Q. Wang, Enhanced visible-light photocatalytic activity of g-C3N4/LaFeO3 heterojunctions for the removal of tetracycline hydrochloride. Diam. Relat. Mater. **132**, 109685 (2023)
12. J. Zhang, Y. Zhao, K. Zhang, A. Zada, K. Qi, Sonocatalytic degradation of tetracycline hydrochloride with CoFe2O4/g-C3N4 composite. Ultrason. Sonochem. **94**, 106325 (2023)
13. Y. Zhao, J. Liu, C. Wang, X. Zhang, C. Chen, X. Zhao, J. Li, H. Jin, Enhanced photocatalytic activity of graphitic carbon nitride synthesized by protonated precursor approach. J. Power. Sources **424**, 176 (2019)
14. Y. Zhang, Q. Pan, G. Chai, M. Liang, G. Dong, Q. Zhang, J. Qiu, Synthesis and luminescence mechanism of multicolor-emitting g-C3N4 nanopowders by low temperature thermal condensation of melamine. Sci. Rep. **3**(1), 1 (2013)
15. A.A. Yadav, S.W. Kang, Y.M. Hunge, Photocatalytic degradation of Rhodamine B using graphitic carbon nitride photocatalyst. J. Mater. Sci. Mater. Electron. **32**(11), 15577 (2021)
16. T. Nakagawa, S. Fujiwara, S. Shimoda, K. Suzuki, A. Fukuoka, T. Takada, Photocatalytic formaldehyde decomposition efficiency of g-C3N4 prepared from melamine/urea mixtures: influence of starting material composition. Chem. Phys. Lett. **850**, 141457 (2024)
17. S. Hassanzadeh, S. Farhadi, F. Moradifard, Synthesis of magnetic graphene-like carbon nitride-cobalt ferrite (gC3N4/CoFe2O4) nanocomposite for sonocatalytic remediation of toxic organic dyes. RSC Adv. **13**(16), 10940 (2023)
18. W. Xucong, D. Hao, J. Zhongyi, Y. Liyong, Photocatalytic reduction of Re (VII) on amorphous TiO2/g-C3N4 derived from different N sources. J. Inorg. Mater. **35**(12), 1340 (2020)
19. X. Zhao, Y. Zhang, X. Zhao, X. Wang, Y. Zhao, H. Tan, H. Zhu, W. Ho, H. Sun, Y. Li, Urea and melamine formaldehyde resin-derived tubular g-C3N4 with highly efficient photocatalytic performance. ACS Appl. Mater. Interfaces **11**(31), 27934 (2019)
20. P. Negro, F. Cesano, A. Damin, R. Brescia, D. Scarano, Porous g-C3N4-based nanoarchitectures by playing with sustainable precursors: Role of urea/melamine ratio on the structure/properties relationship. J. Alloys Compd. **1002**, 175053 (2024)
21. Y. Niu, F. Hu, H. Xu, S. Zhang, B. Song, H. Wang, M. Li, G. Shao, H. Wang, H. Lu, Exploration for high performance g-C3N4 photocatalyst from different precursors. Mater. Today Commun. **34**, 105040 (2023)
22. J. Zhang, T. Cai, H. Li, H. Zhao, Synthesis g-C3N4 of high specific surface area by precursor pretreatment strategy with SBA-15 as a template and their photocatalytic activity toward degradation of rhodamine B. Phosphorus Sulfur Silicon Relat. Elem. **194**(3), 229 (2019)
23. Y. Shen, X. Guo, X. Bo, Y. Wang, X. Guo, M. Xie, X. Guo, Effect of template-induced surface species on electronic structure and photocatalytic activity of g-C3N4. Appl. Surf. Sci. **396**, 933 (2017)
24. Q. Hao, X. Niu, C. Nie, S. Hao, W. Zou, J. Ge, D. Chen, W. Yao, A highly efficient gC 3 N 4/SiO 2 heterojunction: the role of SiO 2 in the enhancement of visible light photocatalytic activity. Phys. Chem. Chem. Phys. **18**(46), 31410 (2016)
25. W. Chen, M. Liu, X. Li, L. Mao, Synthesis of 3D mesoporous g-C3N4 for efficient overall water splitting under a Z-scheme photocatalytic system. Appl. Surf. Sci. **512**, 145782 (2020)
26. S. Wu, N. Zhang, C. Wang, X. Hou, J. Zhao, S. Jia, J. Zhao, X. Cui, H. Jin, T. Deng, An efficient and mild recycling of waste melamine formaldehyde foams by alkaline hydrolysis. Green Energy Environ. **9**(5), 919 (2022)
27. Y. Yang, J. Zhu, Y. He, M. Li, Y. Liu, M. Chen, D. Cao, Charge transfer in photocatalysis of direct Z-scheme g-C3N4-based ferroelectric heterojunction. J. Alloys Compd. **893**, 162270 (2022)
28. Y. Zhong, Z. Wang, J. Feng, S. Yan, H. Zhang, Z. Li, Z. Zou, Improvement in photocatalytic H_2 evolution over g-C3N4 prepared from protonated melamine. Appl. Surf. Sci. **295**, 253 (2014)

29. M.R. Islam, A.K. Chakraborty, M.A. Gafur, M.A. Rahman, M.H. Rahman, Easy preparation of recyclable thermally stable visible-light-active graphitic-C3N4/TiO2 nanocomposite photocatalyst for efficient decomposition of hazardous organic industrial pollutants in aqueous medium. Res. Chem. Intermed. **45**(4), 1753 (2019)
30. R.S. Bhosale, M. Al Kobaisi, S.V. Bhosale, S. Bhargava, S.V. Bhosale, Flower-like supramolecular self-assembly of phosphonic acid appended naphthalene diimide and melamine. Sci. Rep. **5**(1), 14609 (2015)
31. F.Y. Ban, S.R. Majid, N.M. Huang, H.N. Lim, H.N. Lim, Graphene oxide and its electrochemical performance. Int. J. Electrochem. Sci. **7**(5), 4345 (2012)
32. G. Yuhaneka, A.I. Rozafia, W.P. Utomo, A. Iryani, D. Hartanto, Synthesis of porous g-C3N4 and its application as photocatalyst for methylene blue degradation. Malays. J. Fundam. Appl. Sci. **18**(4), 463 (2022)
33. T. Narkbuakaew, P. Sujaridworakun, Synthesis of tri-S-triazine based g-C3N4 photocatalyst for cationic rhodamine B degradation under visible light. Top. Catal. **63**(11), 1086 (2020)
34. X. Qiao, Z. Zhou, X. Liu, C. Zhao, Q. Guan, W. Li, Constructing a fragmentary g-C3N4 framework with rich nitrogen defects as a highly efficient metal-free catalyst for acetylene hydrochlorination. Catal. Sci. Technol. **9**(14), 3753 (2019)
35. X. Jin, X. Fan, J. Tian, R. Cheng, M. Li, L. Zhang, MoS 2 quantum dot decorated g-C3N4 composite photocatalyst with enhanced hydrogen evolution performance. RSC Adv. **6**(58), 52611 (2016)
36. L. Zhang, Z. Jin, H. Lu, T. Lin, S. Ruan, X.S. Zhao, Y.J. Zeng, Improving the visible-light photocatalytic activity of graphitic carbon nitride by carbon black doping. ACS Omega **3**(11), 15009 (2018)
37. P. Cui, Y. Hu, M. Zheng, C. Wei, Enhancement of visible-light photocatalytic activities of BiVO4 coupled with g-C3N4 prepared using different precursors. Environ. Sci. Pollut. Res. **25**(32), 32466 (2018)
38. X.J. Wang, C. Liu, X.L. Li, F.T. Li, Y.P. Li, J. Zhao, R.H. Liu, Construction of g-C3N4/Al2O3 hybrids via in-situ acidification and exfoliation with enhanced photocatalytic activity. Appl. Surf. Sci. **394**, 340 (2017)
39. L. Luo, A. Zhang, M.J. Janik, C. Song, X. Guo, Facile fabrication of metal-free urchin-like gC 3 N 4 with superior photocatalytic activity. RSC Adv. **6**(97), 94496 (2016)
40. Y. Li, S. Yi, R. Duan, S. Li, Z. Sun, J. Shi, L. Gao, Enhanced photocatalytic performance of Na1. 8Zn2. 1Mo3O12/g-C3N4 heterojunction for tetracycline degradation. J. Environ. Chem. Eng. **11**(5), 110471 (2023)
41. G. Rana, P. Dhiman, A. Kumar, E.A. Dawi, G. Sharma, Visible-light driven Z-scheme g-C3N4/Fe-MOF photocatalyst for degradation of organic pollutants. J. Inorg. Organomet. Polym. Mater. **34**(6), 2688 (2024)
42. M. Mousavi, A. Habibi-Yangjeh, M. Abitorabi, Fabrication of novel magnetically separable nanocomposites using graphitic carbon nitride, silver phosphate and silver chloride and their applications in photocatalytic removal of different pollutants using visible-light irradiation. J. Colloid Interface Sci. **480**, 218 (2016)
43. B. Wang, X. Liu, S. Dai, H. Lu, α− Fe2O3 nanoparticles/porous g-C3N4 hybrids synthesized by calcinations of Fe-based MOF/melamine mixtures for boosting visible-light photocatalytic tetracycline degradation. ChemistrySelect **5**(11), 3303 (2020)
44. J. Guo, P. Li, Z. Yang, A novel Z-scheme g-C3N4/LaCoO3 heterojunction with enhanced photocatalytic activity in degradation of tetracycline hydrochloride. Catal. Commun. **122**, 63 (2019)

Authors and Affiliations

Hafize Nagehan Koysuren[1] · Sumyah Amer Yahya[2] · Ozcan Koysuren[2]

✉ Ozcan Koysuren
koysuren@ankara.edu.tr

Hafize Nagehan Koysuren
nagehan.koysuren@ahievran.edu.tr

Sumyah Amer Yahya
somayayahya.rs@gmail.com

[1] Department of Environmental Engineering, Faculty of Engineering and Architecture, Kirsehir Ahi Evran University, 40100 Kirsehir, Turkey

[2] Department of Energy Systems Engineering, Engineering Faculty, Ankara University, 06830 Ankara, Turkey